Compressive stress effects on nanoparticle modulus and fracture

W. M. Mook,[1] J. D. Nowak,[1] C. R. Perrey,[1] C. B. Carter,[1] R. Mukherjee,[2] S. L. Girshick,[2]
P. H. McMurry,[2] and W. W. Gerberich[1]
[1]*Chemical Engineering and Materials Science, 151 Amundson Hall, University of Minnesota, Minneapolis, Minnesota 55455, USA*
[2]*Mechanical Engineering, 111 Church Street, University of Minnesota, Minneapolis, Minnesota 55455, USA*
(Received 24 October 2006; revised manuscript received 4 April 2007; published 22 June 2007)

Individual nanoparticles of silicon and titanium having diameters in the range of 40–140 nm have been repeatedly compressed by a nanoindenter. Even at low loads, the small tip-particle and particle-substrate contacts generate extreme pressures within the confined particle, influencing its stiffness and fracture toughness. The effect of these high pressures on the measured modulus is taken into account by invoking a Murnaghan equation-of-state-based analysis. Fracture toughness of the silicon particles is found to increase by a factor of 4 in compression for a 40-nm-diam particle when compared to bulk silicon. Additionally, strain energy release rates increase by more than an order of magnitude for particles of this size when compared to bulk Si.

DOI: 10.1103/PhysRevB.75.214112 PACS number(s): 62.25.+g, 62.20.Fe, 62.20.Qp

I. INTRODUCTION

A recent trend in nanoindentation has been to evaluate the properties of nanoparticles[1–3] and small structures.[4,5] Typically this has been accomplished by using scanning-probe-microscopy- (SPM-) based nanoindenters in order to locate the structure of interest. Unique issues are encountered with this type of testing; besides adopting new algorithms to determine the proper contact area, what assumptions are necessary in order to calculate modulus when considering the contact of individual nanoscale structures? In these instances, relatively low loads can generate extreme contact pressures that, in turn, can influence the effective local elastic moduli. This is important since when quantifying the early stages of plasticity through to the later stages of fracture, the need for any changes in modulus as a function of pressure is critical.[6–8] Additionally, if one is to design a robust freestanding nanostructure, the fracture toughness needs to be described and this also often requires the knowledge of the elastic modulus.

In general, the extremely high pressures generated at nanoscale contacts can be thought of as happening at the contact between surface asperities. Specific examples of this would include atomic force microscopy (AFM) tips scanning a surface, microelectromechanical system (MEMS) components in contact, and in our case, compression of individual nanoparticles between a diamond indenter tip and sapphire substrate. Numerous experimental and computational results show that when large compressive or tensile stresses develop in materials, the effective elastic modulus is influenced. For example, Jarausch *et al.*[9] used an interfacial force microscope to measure the elastic properties of 100-nm-thick gold films and found that a 50-GPa compressive stress increased the film's effective indentation modulus by 42%. Astala *et al.*[10] combined a quasistatic molecular dynamics simulation with a density-functional-based tight-binding method to investigate indentation into silicon. At small indentation depths, they report hardness values up to 89 GPa and elastic modulus values up to 397 GPa. By measuring acoustic velocities, Wang[11] found stress effects on the modulus of metallic glasses under high pressure. For two glasses with Young's moduli of approximately 100 GPa under zero pressure, compressive pressures of 10 GPa were projected to increase the bulk moduli by 36% and 40%. This pressure effect is also observed for standard nanoindentation into planar films. Veprek and Argon[8] noted that when indenting films with hardnesses appreciably greater than 20 GPa, the modulus measured using the Oliver-Pharr technique[12] will overestimate the material modulus unless the effect of compressive pressure is accounted for. However, the appropriate experimental assessment of how high compressive pressures affect the elastic stiffness in freestanding nanostructures under compression has yet to be done.

Geophysicists have been quantifying the effect of pressure on bulk moduli for decades by using seismic events to investigate the properties of Earth's high-pressure interior, leading to the development of equations of state (EOS). One of the most simple, yet most popular and effective equations of state is the Murnaghan relationship.[13] A basic assumption that can be used to derive this relation is that the bulk modulus is a linear function of pressure for small volume changes, such that

$$K = K_0 + \alpha p, \tag{1}$$

where K is the bulk modulus, K_0 is the zero pressure bulk modulus, α is the bulk modulus pressure first derivative, and p is pressure. This relation has been confirmed using an ever-growing database of experimental seismic[14] and diamond anvil cell[15,16] data. For a full development of the theory see pp. 65 and 77 of Poirier (Ref. 13). The pressure effect on the bulk modulus can be related to the compressive elastic modulus E_0 through Poisson's ratio ν by

$$K_0 = \frac{E_0}{3(1-2\nu)}. \tag{2}$$

One finds from combining Eqs. (1) and (2) that

$$E = E_0 + \beta p, \tag{3}$$

where $\beta=3\alpha(1-2\nu)$. A value of $\alpha\simeq 4$ is found to be valid for many materials[13] and silicon in particular.[17] It will be shown that Eq. (3) is an appropriate way to measure the effective elastic modulus of nanoparticles and nanostructures under compression.

The large contact pressures that are generated in nanoparticles under compression also influence the local fracture toughness and strain energy release rate since both measures depend upon the elastic modulus. While these silicon nanoparticles can accommodate large plastic strain, Nowak *et al.*[3] showed that compression could eventually lead to cleavage-based fracture. This is seen in a movie[3] recorded using a transmission electron microscope (TEM) equipped with an *in situ* indentation holder. Large pressures also promote dislocation behavior, which increases fracture resistance. The propensity for dislocation plasticity is increased in a freestanding structure compared to a planar surface by the decrease in constraint in the structure. With *in situ* TEM indentation of silicon wedges, Minor *et al.*,[18] showed that, after indentation, plastic deformation was due entirely to dislocation plasticity and not to a phase change.

The present study first assesses the pressure effect on modulus of elasticity in 40–140-nm-diameter nanospheres of Si (Ref. 1) and Ti. Those values are then used to determine semiquantitative estimates of the strain energy release rate. It is shown that for brittle nanospheres the experimental procedure is fairly simple; however, the interpretation is complicated due to the deformation history. We want to make it very clear that the phenomena to be discussed are appropriate to extremely small contacts and volumes under compression.

II. ELASTIC MODULUS

When determining elastic moduli using nanoindentation, it is first necessary to make appropriate estimations of the area that is supporting the applied load. In the case of a compressed nanoparticle between two rigid platens, both upper and lower bound estimates of the contact area are considered. An estimate of the minimum area supporting the compressive load would be the contact area between platens and particle. This estimate, detailed below, assumes a geometric contact area with a uniform pressure within it. The modulus can then be calculated assuming the particle unloads elastically. Alternatively, the maximum possible area supporting the load would be the nanosphere's midplane. This is calculated using a cylindrically shaped particle based on constancy of volume of the particle in both its initial and compressed states. For this approach, the modulus is calculated using an average true-stress–true-strain relationship. These models are applied to both silicon and titanium nanospheres.

A. Contact area models

Estimating contact area as a function of displacement is necessary for nanoindentation. During standard nanoindentation of thin films, the indentation surface is assumed to be flat. And thus by indenting a material with known properties such as fused quartz, the contact area as a function of displacement can be calculated. Unfortunately this approach is not applicable to the compression of individual nanospheres where the indenter tip has a much larger radius of curvature than the particle or structure that is being indented. However, contact models between spheres and flat surfaces have a long, well-developed history in continuum mechanics beginning with Hertz.[19] The Hertzian contact radius a_H is

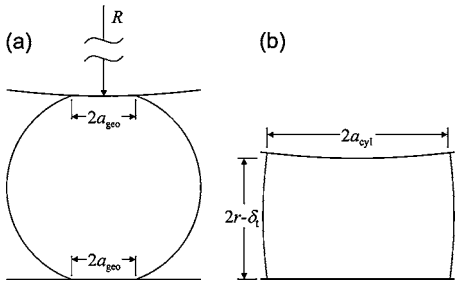

FIG. 1. Schematics depicting contacting radii used in determining stress for (a) mean contact pressure as an upper-bound stress and (b) average stress in an equivalent height right cylinder as a lower-bound stress.

$$a_H = (\delta r)^{1/2}, \tag{4}$$

where δ is the displacement at one contact and r is the reduced contact radius. In the case of a nanoparticle being compressed between a large-radius diamond tip and sapphire substrate, the total displacement measured by the nanoindenter, δ_t, would be divided in half to satisfy the condition of one contact elastically deforming. Hertzian theory assumes that the spheres are isotropic, the contact radius and deformation are small when compared to the reduced radius of curvature of the system, and the deformation is elastic. However, the compressions of the nanospheres, even at small displacements, are characterized by elastic-plastic loading followed by elastic unloading. Considering that the loading is elastic-plastic, a generously large estimate of the contact radius would be one that uses a purely plastic, geometric contact radius a_{geo}, such that

$$a_{geo} = \left(\delta_t r - \frac{\delta_t^2}{4}\right)^{1/2}, \tag{5}$$

where δ_t is the total displacement measured by the nanoindenter and r is the radius of curvature of the nanosphere. This equation is appropriate at small to intermediate deformations where plastic flow is occurring and is a factor of 2 smaller than a standard geometric radius since the displacement here accounts for both the tip-sphere and sphere-substrate contacts. Additionally, both tip and substrate are assumed to be rigid. A schematic of this situation can be seen in Fig. 1(a).

The second model takes into account that at larger displacements the sphere becomes more barrel shaped and approaches a right cylinder compressed between two platens as seen in Fig. 1(b). At this point fracture is a possibility and the appropriate area that is supporting the load would be associated with the midplane of the sphere. This radius is based on

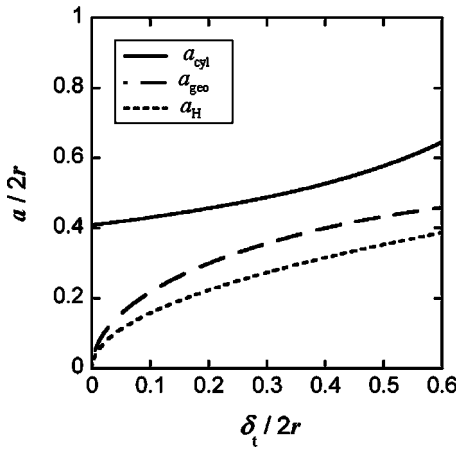

FIG. 2. Values of contact radius a from Eqs. (4)–(6) as a function of total displacement normalized by the initial particle diameter.

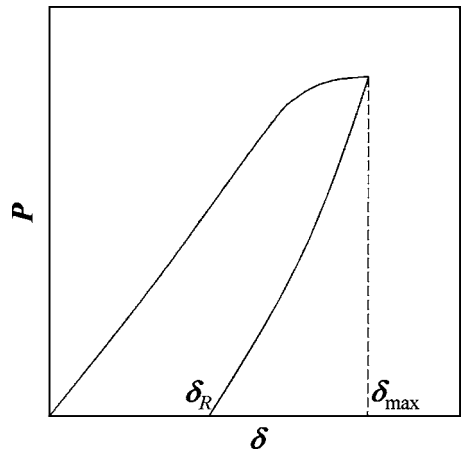

FIG. 3. The elastic unloading displacement $\delta_{max}-\delta_R$ is shown.

a cylinder under compression and is estimated by setting the original volume of the sphere equal to the current volume of the cylinder (cross-sectional area multiplied by the current height). This cylindrical contact radius a_{cyl} is

$$a_{cyl} = \left(\frac{4r^3}{3(2r-\delta_t)}\right)^{1/2}. \tag{6}$$

Figure 2 compares the three contact radii equations above versus displacement, with both axes normalized by initial particle diameter. The Hertzian radius is only valid for elastic deformations at small displacements. Since the majority of modulus measurements are taken at total displacements between 20% and 60% of the initial diameters of the particles, a relatively narrow spread between the geometric contact and cylindrical midplane radii is used in the modulus estimates.

B. Pressure-enhanced elastic modulus models

First consider how one might treat a sphere that was compressed (elastic-plastic loading and elastic unloading) using a uniform pressure contact stress. For an analysis of the contact stress, we consider a mean pressure applied to a circular region of contact, πa_{geo}^2, as seen in Fig. 1(a). As shown by Johnson,[22] the mean displacement of a single circular contact under uniform pressure is given by

$$\bar{u}_z = \frac{16pa}{3\pi E^*}, \tag{7}$$

where p is a uniform pressure, a is the contact radius, in this case a_{geo}, and E^* is the reduced modulus. Since the elastic displacement is assumed to be equally divided between the top and bottom contacts of the sphere in Fig. 1(a), for large tip radii R, we can approximate an upper-bound modulus assuming only the contact regions to unload as in the rigid punch approximation, giving

$$E^* = \frac{32P}{3\pi^2 a_{geo}\delta_E^u}. \tag{8}$$

Here, the pressure p is $P/\pi a_{geo}^2$, where P is the load and δ_E^u is the elastic unloading displacement that occurs at both the top and bottom contacts of the sphere. Experimentally, δ_E^u, is taken as the maximum displacement minus the residual displacement ($\delta_{max}-\delta_R$) as shown in Fig. 3. It will be seen that Eq. (8) represents an upper bound for the modulus, $E^*=E_{ub}^*$, even with the use of the perfectly plastic a_{geo} and the large "rigid punch" unloading displacement, and as such overestimates the stiffness of the entire sphere leading to moduli well beyond expectations.

The second model takes into account that at larger displacements the sphere becomes more barrel shaped and approaches a right cylinder compressed between two platens. The simple geometric construct for the right cylinder in Fig. 1(b) assumes the cylinder is compressed an equal amount from top and bottom with the upper and lower platen areas $\bar{A}$ represented by πa_{cyl}^2. We propose this as an appropriate estimate of the average cross-sectional area supporting the load. As such, an average true compressive stress $\bar{\sigma}$ is obtained by dividing the load P by the above area. To obtain an average true elastic unloading strain $\bar{\varepsilon}_E^u$, the unloading elastic displacement δ_E^u is divided by the current cylinder height. This is given as

$$\bar{\varepsilon}_E^u = \frac{\delta_E^u}{(2r-\delta_t)}. \tag{9}$$

Since we now have an average true stress and an average true elastic unloading strain, the elastic modulus may be estimated. This gives

$$E_{lb} \approx \frac{\bar{\sigma}}{\bar{\varepsilon}_E^u} = \frac{3P(2r-\delta_t)^2}{4\pi r^3 \delta_E^u}, \tag{10}$$

where the "lb" subscript indicates that this represents a lower-bound estimate. Since the numerical coefficients in both Eqs. (8) and (10) are nearly unity for small displacements, the distinguishing features for these equations are

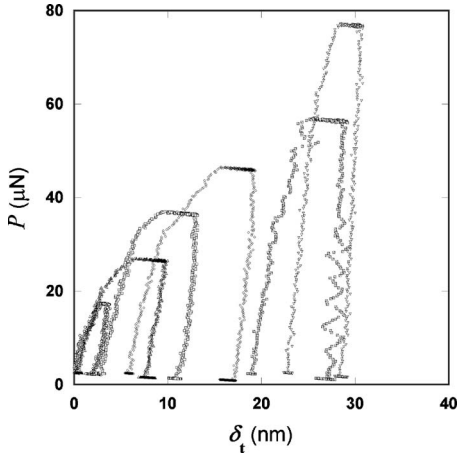

FIG. 4. Repeat compression loadings of a 44-nm silicon sphere. Note the jump in cumulative displacement between the 45-μN and 55-μN runs.

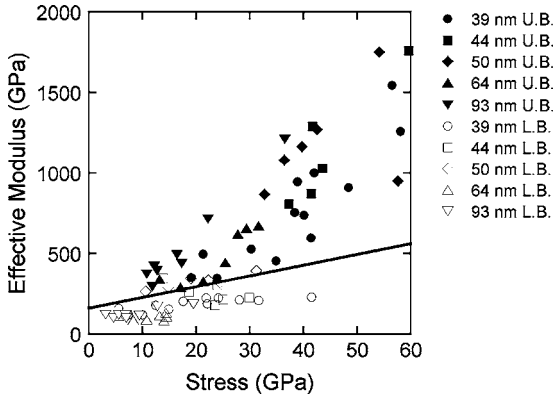

FIG. 5. Modulus estimates for different diameter silicon nanospheres using a right-cylinder approximation (open symbols) for average bearing area giving lower-bound moduli and a rigid punch approximation using an average contact area (solid symbols) giving upper-bound moduli.

$1/\sqrt{\delta r}$ for Eq. (8) vs $1/r$ for Eq. (10). As δ_t becomes large, these two equations would again diverge. In the range of interest then, the lower- and upper-bound stresses have area estimates ranging by slightly more than a factor of 2. It is clear that Eq. (8) will lead to much larger moduli as only the contact stress is considered rather than the average stress in the body, but it is not as clear that Eq. (10) is always a lower bound. However, for both estimates we have been conservative in considering the elastic unloading to be the fully recovered displacement rather than just the unloading slope. Further, we did not adjust this apparent modulus for any displacement associated with the upper and lower platens.

C. Modulus measurements of silicon nanospheres

As explained elsewhere,[5] an aerodynamically focused beam of nanoparticles formed directly from a thermal plasma was deposited as a line on a sapphire substrate. Isolated particles at the edge of the line were imaged with SPM-based nanoindenters (TriboScope, TriboIndenter, Hysitron, Inc., Edina, MN). In this way heights of nanoparticles could be measured before and after each compression. A series of load-displacement curves for a 44-nm-diameter nanosphere of Si can be seen in Fig. 4. For each subsequent run it is seen that the load increases rapidly for a given displacement partially due to an increased contact area and partially due to work hardening. Overall, the contact pressures and mean stresses in the sphere increase for each run. The large increase in cumulative displacement between the loading runs of 45 μN and 55 μN in Fig. 4 is associated with sphere fracture, similar to the TEM-indentation fracture of a silicon nanoparticle by Nowak *et al.*[3] With regard to load bearing capability, it was observed that the 44-nm silicon sphere supports equivalent loads compared to larger (93-nm-diameter) spheres at the same displacement, implying much larger stresses in the smaller sphere due to roughly a factor of 4 smaller contact area.

Prior to each compression the height of the particle is measured which is indicative of how much permanent displacement has remained from the previous run. With this, the total, or cumulative, displacement can be determined at any displacement in the subsequent run and represents the value of δ_t used in Eqs. (5), (6), (9), and (10). The elastic unloading displacement δ_E^u in Eqs. (8)–(10) is the displacement at maximum load minus the residual displacement at zero load of the unloading curve. Calculated values of E_{ub}^* and E_{lb} from Eqs. (8) and (10) are given in Fig. 5, as a function of normal stress for repeat compressions of five silicon particles with diameters in the range of 39–93 nm. A linear least-squares fit with the same functional form as Eq. (3) for the upper-bound pressure-enhanced modulus values of Eq. (8) extrapolates to a zero pressure value of E_0=160 GPa, but at higher pressures increases with a coefficient of β=19.2 to unrealistic values. The contact stress values may be correct; however, the contact area is not representative of the area responsible for supporting the load once large deformations take place. At large deformations, the entire sphere, not just the portions under contact, would be elastically unloading. Therefore, for silicon particles with mean contact stresses below 10 GPa, Eq. (8) is valid. However, for larger contact stresses, the equation should only be considered an upper-bound estimate.

The linear least-squares fit of the lower-bound pressure-enhanced modulus estimate, E_{lb}, of Eq. (10) extrapolates to E_0=80 GPa at zero pressure and increases at higher pressures with a coefficient of β=6.45. The lower-bound estimate of Eq. (10) generates unrealistically low modulus values at small displacements and pressures since it calculates stress using the radius of an equivalent cylinder, a_{cyl}, which is unrealistically large at small displacements as seen in Fig. 2. However the pressure coefficient of 6.45 agrees well with the Birtch-Murnaghan coefficient for silicon,[17] which after substitution into Eq. (3), using ν_{Si}=0.218 and α=4, produces β_{Si}=6.67. Given that similarity, we considered the best representation of the compressive stress effect on the effective modulus of silicon nanoparticles to be

$$E_{Si} = 160\ \text{GPa} + 6.67\bar{\sigma}. \tag{11}$$

This equation is represented in Fig. 5 and has the satisfying aspect that all of the upper-bound calculations are above the

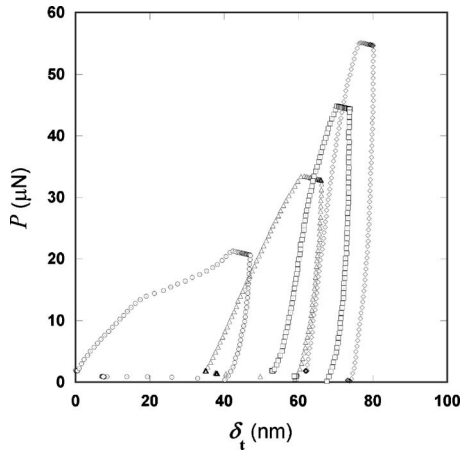

FIG. 6. Repeat compression loadings of a 143-nm-diameter titanium sphere. A large amount of plastic flow occurred during the first compression. However, there is not compelling scanning probe microscopy or displacement excursion evidence that the nanoparticle fractured.

trend line and nearly all of the lower-bound estimates are below the trend line.

D. Modulus measurements of titanium nanospheres

Measurements similar to those for silicon resulted in the load-displacement curves for a series of titanium nanospheres. An example of repeat compressions of a 143-nm-diameter Ti nanosphere can be seen in Fig. 6. As with silicon, there is a large increase in both upper and lower bounds of the apparent modulus for the titanium nanospheres with increasing superimposed stress as seen in Fig. 7. Using $E_0=105$ GPa as the extrapolation point for the upper-bound linear fit gives a pressure coefficient of $\beta=12.6$ which is too large to be realistic. On the other hand, for the lower bound, the least-squares coefficient of $\beta=4.5$ agrees reasonably well with the Birtch-Murnaghan coefficient of titanium[21] using $\nu_{\mathrm{Ti}}=0.321$ and $\alpha=3.8$, to produce a value of $\beta_{\mathrm{Ti}}=4.1$. The

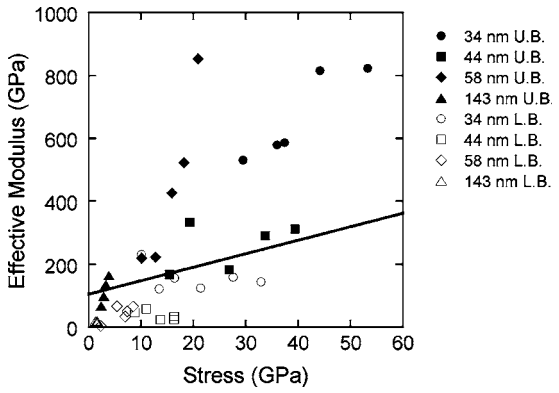

FIG. 7. Modulus estimates for different diameter titanium nanospheres using a right-cylinder approximation (open symbols) for average bearing area giving lower-bound moduli and a rigid punch approximation using an average contact area (solid symbols) giving upper-bound moduli.

lower-bound intercept at zero pressure is $E_0=20$ GPa. As with silicon, the moduli based on the lower-bound estimate at low pressures are well below the accepted modulus of Ti at zero pressure which is 105 GPa. Therefore the following is used as the best estimate of the effect of superimposed compressive stress on the modulus of titanium nanospheres,

$$E_{\mathrm{Ti}} = 105\ \mathrm{GPa} + 4.3\bar{\sigma}. \tag{12}$$

This Birtch-Murnaghan-style relation produces the line in Fig. 7 where all lower-bound estimates except one fall below the line and all upper-bound estimates except three are above the line. Additional information on the plasticity response of the Ti nanoparticles can be found elsewhere.[22]

E. Pressure-enhanced modulus discussion

The modulus estimates for both the silicon and titanium nanoparticles detailed above show large amounts of scatter. There is nearly a factor of 2 scatter at all levels of compressive pressure for the lower-bound modulus estimate and slightly more for the upper-bound estimate of Figs. 5 and 7. Such scatter is not related to any length-scale effect since, for a given stress level the smallest spheres are intermixed with the largest. Rather, the scatter is partially associated with the repeatability of accurately returning the tip to the top of the particle prior to each run, which will affect the calculated cumulative displacement. Furthermore, from sphere to sphere the crystallographic axis of deformation will be different which will also influence the relative stiffness. Given these uncertainties and the nanometer-level displacements measured, such scatter is expected.

The modulus measurements are conservative in nature since we did not consider any displacement accommodation by the diamond tip or sapphire substrate. Both platens would be influenced by the high pressures and would share a portion of the unloading displacement. From experiments currently in progress we know that some displacement accommodation is taking place at loads in the 30–60 μN range. This will clearly increase the nanoparticle modulus magnitudes of both estimates. Once additional confidence is gained regarding the partitioning of displacement, even larger displacements and attendant pressures should be possible.

As an additional check to confirm that this approach to moduli is reasonable, consider the elastic portion of the initial compression of a silicon nanoparticle where the load-displacement curve should follow a Hertzian relationship. In this case, using Hertzian theory, it is possible to be more exact concerning the tip-particle-substrate deformation. A 46-nm-diameter silicon sphere was imaged before and after compression with scanning electron microscopy (SEM) as seen in Figs. 8(a) and 8(b). The compression was conducted under displacement control at a loading rate of 1 nm/s. The Hertzian load-displacement relationship is

$$P = \frac{4}{3}E^* r^{1/2}\delta^{3/2}, \tag{13}$$

where the radius r is the radius of the particle and not the average of the reduced radius of the two contacts, since the reduced radius of tip (in this case a 5-μm conical diamond)

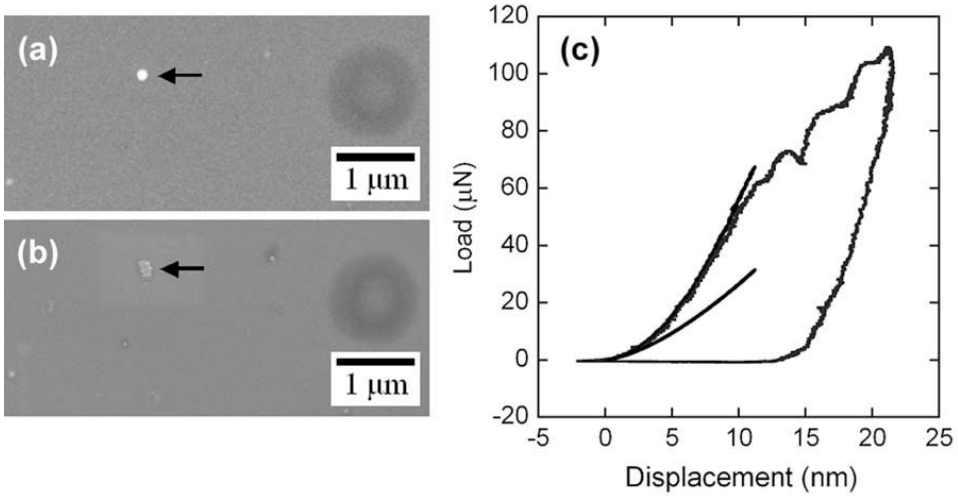

FIG. 8. Compression of a 46-nm-diameter silicon nanoparticle with load control at a rate of 1 nm/s where (a) is the precompression and (b) the postcompression SEM image of the particle. (c) Hertzian relationships are superimposed on the load-displacement data using the standard modulus (under predicting relationship) and pressure-enhanced modulus for the tip, particle, and substrate.

and the particle (23 nm) is 22.9 nm. The effective reduced modulus E^* is the average of the tip-particle and particle-substrate reduced moduli such that

$$E^* = \frac{E_1^* + E_2^*}{2}, \quad \frac{1}{E_1^*} = \frac{1-\nu_{\mathrm{Si}}^2}{E_{\mathrm{Si}}} + \frac{1-\nu_{\mathrm{Al_2O_3}}^2}{E_{\mathrm{Al_2O_3}}},$$

$$\frac{1}{E_2^*} = \frac{1-\nu_{\mathrm{Si}}^2}{E_{\mathrm{Si}}} + \frac{1-\nu_{\mathrm{dia}}^2}{E_{\mathrm{dia}}}. \tag{14}$$

Now, if one does not consider the effect of compressive pressure on the effective modulus and uses the following values for the zero-pressure moduli and Poisson's ratio for silicon (160 GPa, 0.22), sapphire (375 GPa, 0.29), and diamond (1007 GPa, 0.07), then Eq. (13) produces the fit in Fig. 8(c) that vastly underpredicts the elastic load-displacement response. If, however, the influence of pressure within the silicon nanoparticle is accounted for, Eq. (13) does reproduce the elastic response in Fig. 8(c). For this fit, the pressure-enhanced silicon modulus follows Eq. (11) with the pressure taken to be the average of the geometric contact and right cylinder stress estimates, such that

$$\bar{\sigma} = \frac{\bar{\sigma}_{\mathrm{geo}} + \bar{\sigma}_{\mathrm{cyl}}}{2}, \quad \bar{\sigma}_{\mathrm{geo}} = \frac{P}{\pi a_{\mathrm{geo}}^2}, \quad \bar{\sigma}_{\mathrm{cyl}} = \frac{P}{\pi a_{\mathrm{cyl}}^2}. \tag{15}$$

The pressure coefficient to produce this fit is $\beta_{\mathrm{Si}}=5.8$, which equates to a value of $\alpha_{\mathrm{Si}}=3.4$, approximately 15% lower than the standard value of 4.0 [see Eq. (1)]. It is thought that this difference may be due to the large proportion of nonhydrostatic stress within the particle from the uniaxial compression as compared to standard diamond-anvil cell experiments. With that said, the pressure-enhanced modulus approach shows much more promise than the non-pressure-enhanced Hertzian load-displacement relationship seen in Fig. 8(c) that drastically underpredicts the experimental data.

III. FRACTURE TOUGHNESS AND STRAIN ENERGY RELEASE RATE

Having an estimate of elastic modulus for silicon nanoparticles, we proceed to examine their fracture behavior. Fracture of these particles is confirmed using a combination of *in situ* SPM images and load-displacement discontinuities. Where available, *ex situ* AFM and SEM images will be referenced as well. As there was not compelling evidence that the titanium nanospheres fractured, they are not considered. Additional *in situ* TEM compression of a silicon nanoparticle by Nowak *et al.*[3] gives direct evidence of the brittle nature of nanoparticle fracture. They show that the particle first deforms elastically with quantitatively equal amounts of deformation at both the tip-particle and particle-substrate contacts. This is followed by plastic deformation and cleavage fracture along a favorably oriented (111)-type plane. An image of the nanoparticle after the compression and fracture event can be seen in Fig. 9. With this evidence, we first outline a model for the local stress nucleating fracture and a method for converting that to a fracture toughness and strain energy release rate. These are then compared to the stored elastic energy in the sphere that is released upon fracture.

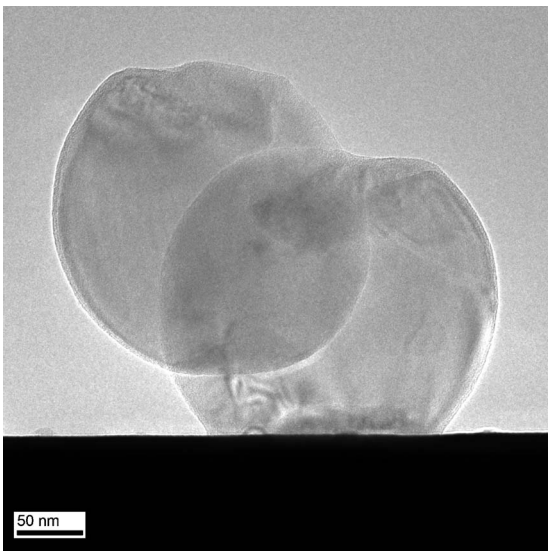

FIG. 9. Bright-field TEM image of a fractured silicon nanoparticle after *in situ* compression as detailed in Ref. 3. The particle fractured into two pieces, one of which pulled away from the substrate as the tip was retracted.

A. Fracture stress and fracture toughness

Determining the fracture stress and fracture toughness was thought to be possible if the onset of nanoparticle fracture could be measured. One has the macroscopic Brazilian disk test history,[20,23] for example, to know that compressed ceramic cylindrical disks can give good estimates of fracture toughness. However, defining the stress and crack length is not so simple. Two prior studies are significant: that of Shipway and Hutchings[24] who did a detailed theoretical analysis of the fracture of brittle spheres under compression and that of Majzoub and Chaudhri[25] who visualized low-velocity impact cracking of brittle spheres. Shipway and Hutchings[24] concluded that the only tensile surface stresses responsible for brittle fracture were σ_θ tensile stresses just outside the contact area which might lead to ring cracks or a maximum σ_ϕ acting along the equator. Larger internal tensile stresses did develop for a contact radius to particle radius ratio less than 0.6, leading them to conclude that for large specimens there tended to be an internal defect to nucleate a crack. They proposed that a conservative estimate of the fracture stress was given by

$$\sigma_f^* = 0.4\left(\frac{P}{\pi r^2}\right). \tag{16}$$

Initially, we used this and concluded that it underestimated the stresses responsible for fracture. An alternative approach focused on the fracture of PMMA spheres[25] showing a high-speed photographic sequence that pinpointed the fracture initiation site. The initiation site was found to be at the edge of the contact radius at or near the surface. Given this, we propose a fracture stress criterion based on the mean pressure of the contact using the geometric contact radius from Eq. (15).

As brittle fracture requires a tensile stress and this is compressive, one needs to show that equivalent tensile stresses which are equal but opposite in sign to the mean pressure can evolve. Because of the imperfect loading of these nanospheres, tangential forces will develop, leading to large compressive stresses on one side of the contact edge and equally large tensile stresses on the other.[20] Such contact edge tensile stresses could easily be as large as the mean contact pressure. Using $\bar{\sigma}_{geo}$ from Eq. (15) as an estimate of the stress, the fracture toughness can be determined assuming a defect in the less-tough oxide film coating the nanoparticle. With a free surface magnification factor of 1.1, to first order this becomes

$$K_{Ic} = 1.1\bar{\sigma}_{geo}\sqrt{\pi c}, \tag{17}$$

where c is the defect size. With this determination of K_{Ic}, the strain energy release rate for a fractured silicon particle, can be evaluated with the use of Eq. (11) from

$$G_{Ic} = \frac{K_{Ic}^2}{E_{Si}}, \tag{18}$$

where the E_{Si} values is calculated using Eq. (11) with the appropriate $\bar{\sigma}$ value from Eq. (15) at the load and displacement position where fracture is confirmed in each particle. Given the first-order nature of this calculation, the Poisson term normally used in Eq. (18), $(1-\nu^2)$, is ignored. This

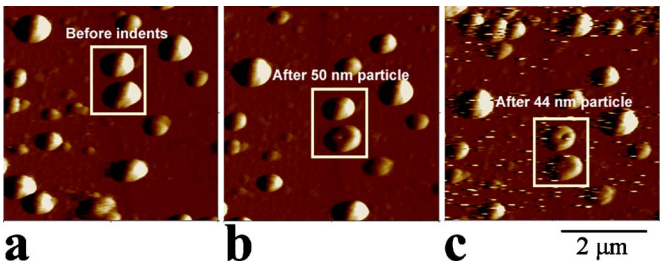

FIG. 10. (Color online) Deflection-mode images of two nanoparticles fractured by repeat loadings to ever-increasing maximum loads as in Fig. 4 showing (a) 50- and 44-nm-diameter spheres imaged with a 1-μm-radius diamond tip (b) after the 50-nm particle was fractured and (c) after the 44-nm particle, the loading of which is seen in Fig. 4, was fractured.

strain energy release rate should be closely linked to the stored elastic energy in the sphere divided by the fracture area. Again, to first order this is just the average elastic strain energy density $\bar{\sigma}^2/2E$ times the volume-to-area ratio of the sphere, V/A_f, where A_f is the new fracture surface created. This becomes

$$\frac{U_E}{A_f} = \frac{\bar{\sigma}^2}{2E}\frac{V}{A_f} = \frac{\bar{\sigma}^2}{2E}\frac{V}{2\pi r^2} = \frac{\bar{\sigma}^2 r}{3E_{Si}}, \tag{19}$$

where the average compressive stress $\bar{\sigma}$ is defined in Eq. (15), the pressure-enhanced effective modulus of silicon, E_{Si}, is defined in Eq. (11), and r is the particle radius. The extra factor of 2 in the denominator accounts for both newly created fracture surfaces. These determinations for fracture resistance are used with the Si nanosphere data as described in the following section.

B. Fracture measurements in silicon nanospheres

Geometric deconvolution reconstructions were made to validate that the contact of other particles were not involved during an individual compression, and as fracture ensued, that the diamond tip did not contact the sapphire substrate. This was facilitated by a series of SPM images using both height- and deflection-mode capabilities. The load at which fracture occurred for a specific silicon nanoparticle is determined by using SPM evidence along with displacement jumps between the runs. Evidence for fracture is shown in Fig. 10(a) which is a deflection image of two particles of interest, 50-nm- and 44-nm-diameter silicon nanospheres. The 50-nm particle was loaded 8 times to consecutively higher maximum loads. After this loading sequence the dimple shown in Fig. 10(b) in the middle of the sphere clearly demonstrated the sphere had fractured. Remembering that these spheres were loaded with a large radius diamond, the only way such a dimpled feature can emerge is for the particle to separate. Adjacent to that sphere, the slightly smaller 44-nm sphere was loaded next. After the fourth compression to 45 μN in Fig. 4, the particle failed which was accompanied by a large decrease in the measured height after the compression. Evidence of this fracture can be seen comparing the upper particle in the outlined area of Figs. 10(b) and 10(c). Pinpointing the actual fracture stress was only

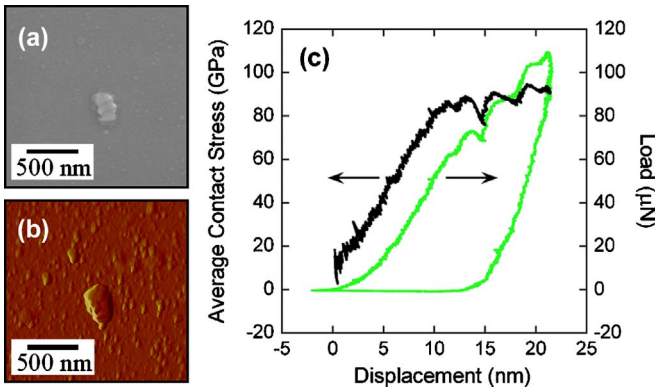

FIG. 11. (Color online) Fractured silicon nanoparticle from Fig. 8 with (a) a post-compression SEM and (b) the corresponding deflection-mode AFM image of the particle which has fractured into at least three pieces. (c) The average contact stress, which is superimposed on the load-displacement curve, levels out once the fracture events (load drops) begin.

crudely accomplished as the loads were increased in 10-μN increments. However, due to increasing contact area, the fracture stress used in Eq. (16) only varied by ±3% from 35 to 55 μN for the 44-nm particle and by ±10% from 45 to 45 μN for the 50-nm particle.

Additional *ex situ* electron microscopy images are used to confirm nanoparticle fracture. Figure 11 reexamines the compressed silicon particle from Fig. 8. Both SEM [Fig. 11(a)] and AFM deflection [Fig. 11(b)] images show this nanoparticle fractured into at least three sections. Using Eq. (15), the average geometric contact stress is superimposed on the load-displacement curve of the fractured particle in Fig. 11(c). Since this particle was loaded using displacement control,[26] fracture events will be evident as load drops instead of displacement discontinuities as seen in Fig. 4. While it is not clear which load drops are responsible for the multiple-fracture events, it is evident that once the load drops and plastic flow begin to occur, a rather constant average peak contact stress state near 85 GPa is maintained.

With the loads and stress necessary for fracture determined, K_{Ic} values were calculated using Eq. (17). To accomplish this, a number of measurements of the oxide film thickness were made by TEM on both the silicon and titanium nanoparticles in Fig. 12. In general, larger-diameter particles had larger film thicknesses. This might be expected since larger particles have a larger residence time and oxygen accumulated during growth would tend to segregate to the surface if the solubility limit is exceeded. With this, we propose that the maximum stress at the edge of the contact fractures the oxide film such that the critical defect size in Eq. (17) is the oxide film thickness, $c=t_{ox}$, from the least-squares line. As this is in the square root of Eq. (17), it should give a first-order estimate of the fracture toughness. Appropriate data are shown in Table I, and values of K_{Ic} versus inverse particle radius are shown in Fig. 13. With this type of plot, one can extrapolate to the bulk fracture toughness which appears to emerge at a particle diameter of 154 nm. Whether this would translate as the transition to small volume effects for fracture of silicon is dependent on how well a linear

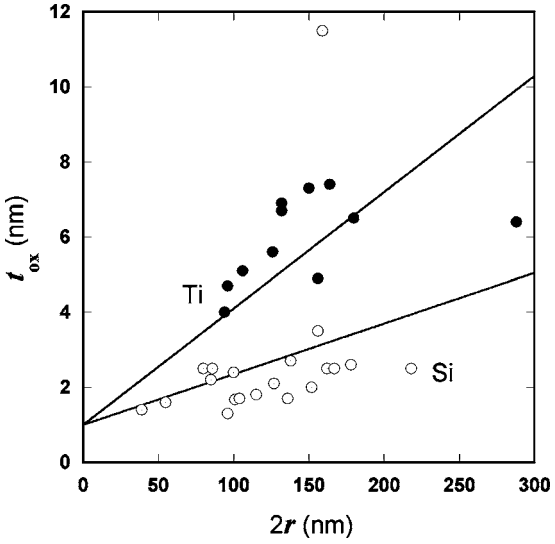

FIG. 12. Measured oxide film thicknesses in different size titanium and silicon nanospheres. Taken using bright-field TEM images on a Philips CM30.

extrapolation to the bulk fracture toughness of 0.8 MPa $m^{1/2}$ represents the fracture mechanism. As a comment on the choice of oxide film thickness as an appropriate defect size, one sees in Fig. 13 that the larger nanoparticle tested *in situ* in the TEM falls on the accepted fracture toughness value for bulk single-crystal silicon of 0.8 MPa $m^{1/2}$. If the oxide film thickness was not a correct measure of the defect that initiated fracture, this data point would have fallen elsewhere. For that reason we strongly suggest that film thickness is a reasonable estimate of the initiating defect size in the context of the scatter shown in Fig. 12. It should be noted that the fractured particle detailed in Figs. 8 and 11 produced a fracture toughness of approximately 6.4 MPa $m^{1/2}$ which is much larger than the data in Fig. 13. This particular nanoparticle had a thin coating of atomic layer deposition (ALD) alumina deposited over it, and as such it is in a different class from the nanoparticles evaluated in Fig. 13. Additional evaluations are currently underway to explore the repeatability and, if found, significance of such a coating.

C. Discussion of strain energy release rates

In the above discussion of fracture toughness, it was suggested that the elastic strain energy release rate G_{Ic} from Eq. (18) could be compared to the stored elastic strain energy times the volume to fracture area ratio of the sphere giving Eq. (19). It is emphasized that these are different estimates since the former uses the average contact stress determined from the geometric contact radius, while the latter uses the average stress in Eq. (15). Such a comparison, as seen in Table I and Fig. 14(a), indicates that the estimate for G_{Ic} is approximately 20% larger than U_E/A_f. Given the assumptions these are in good agreement, and therefore additional discussion uses the fracture toughness estimate of Eq. (17) as representative of the silicon nanosphere fractures. Using this for comparison, G_{Ic} as a function of particle diameter is given in Fig. 14(b). First, as might be expected, a straight

TABLE I. Data for the compression of silicon nanoparticles.

$2r$ (nm)	P (μN)	δ_t (nm)	$\bar{\sigma}_{geo}$[a] (GPa)	$\bar{\sigma}$[a] (GPa)	E_{Si}[b] (GPa)	t_{ox}[c] (nm)	K_{Ic}[d] (MPa·m$^{1/2}$)	U_E/A[e] (J/m^2)	G_{Ic}[f] (J/m^2)	G_{Ic}[g] (J/m^2)
39	55	21	58.3	45.1	461	1.4	4.3	28.7	39.3	117
44	45	18	45.5	35.9	399	1.4	3.3	23.6	27.6	50
50	55	23	39.5	31.1	367	1.5	3.0	21.9	24.2	75
64	45	24	23.0	18.1	280	1.6	1.8	12.4	11.5	39
93	55	36	13.0	10.2	228	1.9	1.1	7.1	5.4	51
216[h]	49	29	5.6	3.7	184	5.4	0.8	2.6	3.5	4
46[i]	73	13	85.0	66.1	601	1.5	6.4	55.8	68.5	26

[a]Equation (15).
[b]Equation (11).
[c]Estimate from Fig. 12.
[d]Equation (17).
[e]Equation (19).
[f]Equation (18).
[g]Equation (24).
[h]From Fig. 9 and Ref. 3.
[i]particle coated with alumina ALD in Figs. 8 and 11.

line extrapolation to 3.5 J/m^2, representative of bulk Si with a modulus of 160 GPa, gives a cutoff of 160 nm consistent with the K_{Ic} extrapolation. If these data are truly representative of the size scale on small volume fracture, what is the possible origin of a d^{-2} dependence? On average, these particles were deformed 45% prior to fracture if we use $\delta_t/2r$ as a measure of strain. This amount of deformation encompasses a large number of dislocations which could represent crack-tip shielding even if the dislocations were not emitted from the crack in the oxide film. The implicit assumption is that the dislocations emitted from the contact edge of the indenter are of the shielding type rather than being antishielding. Assuming these to be shielding gives a shielding stress intensity of[27]

$$k_D = -N\frac{3\mu b}{2(1-\nu)}\frac{\sin\theta\cos(\theta/2)}{(2\pi\bar{x})^{1/2}}, \tag{20}$$

where $\bar{x}$ is the average distance of all shielding dislocations from the crack tip. Taking a typical angle θ between the crack plane and the activated slip planes to be about 30° and assuming that at most $\bar{x}\approx d/2$, one could calculate k_D if the net number of shielding dislocations were known. From previous work,[27] we estimated the number of dislocations that were generated during nanoparticle compression based upon prismatic punching even though we are assuming here that the shielding dislocations are shear loops. The number of dislocations increases due to both increasing displacement and an increasing number of glide cylinders activated, giving

$$N = \frac{\delta}{b}\frac{\gamma a}{r}, \tag{21}$$

where a is the contact radius and γ is a coefficient near unity. Interpreting a in terms of the cumulative displacement and the sphere radius, one can show from Eqs. (20) and (21) that the shielding stress intensity is

$$k_D \simeq -\frac{E\delta\gamma a}{7rd^{1/2}}. \tag{22}$$

The resistance to crack growth as a work per unit fracture area is proportional to k_D^2/E. Crudely, then, one might expect

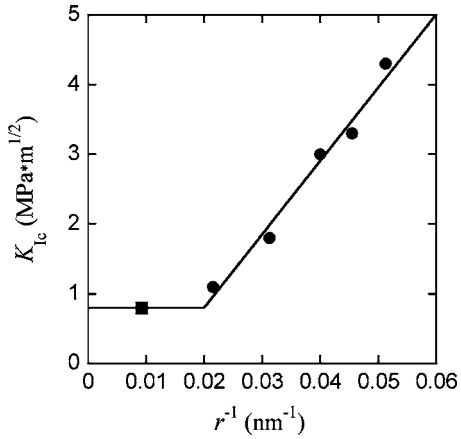

FIG. 13. Fracture toughness from Eq. (17) as a function of inverse particle radius extrapolated to the bulk value of 0.8 MPa m$^{1/2}$ where the value represented as the square is the *in situ* TEM compression from Ref. 3.

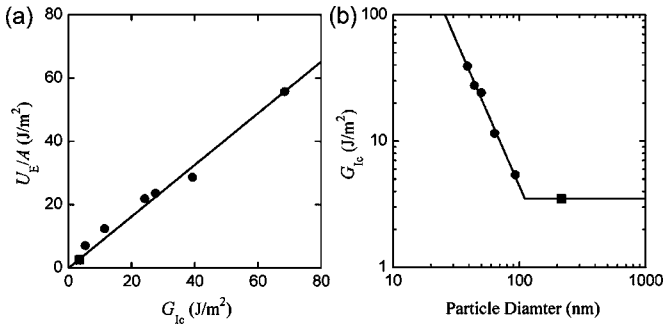

FIG. 14. (a) Comparison of elastic strain energy release rate from Eq. (18) to the stored elastic energy in the particle divided by the fracture area from Eq. (19) where the slope of the least-squares fit is 0.8. (b) Strain energy release rate from Eq. (18) as a function of particle diameter with a cutoff at the bulk property value. The square data point is in reference to the particle shown in Fig. 9 and is detailed in Ref. 3.

$$G_{\mathrm{Ic}} \sim \frac{k_{\mathrm{D}}^2}{E} \sim \frac{2E\delta^2 a^2}{49d^3}, \tag{23}$$

if γ is on the order of 1. As shown in Table I, there is a rough correlation between this shielding estimate and that determined from K_{Ic}. Finally, if we use the first-order geometric relationship between contact radius, particle radius, and displacement, $a^2 \sim \delta r$, one finds from Eq. (23)

$$G_{\mathrm{Ic}} \sim \frac{E\delta^3}{24d^2}, \tag{24}$$

which does represent the d^{-2} dependence shown in Fig. 14(b). The reason that this overestimates the magnitude of G_{Ic} lies with the uncertainty of how many dislocations are shielding and the exact relation between them and the crack tip since the particles' crystallographic orientation varies from particle to particle and γ is unknown. As such, this qualitative agreement is highly speculative and awaits further confirmation from additional studies since other dissipation processes may be involved.

IV. CONCLUSIONS AND SUMMARY

Length-scale effects for nanospheres in compression are found for both modulus of elasticity and fracture toughness. Moduli of silicon and titanium nanospheres increase with increasing mean pressure, approximately following Murnaghan's equation of state.[13] At similar strain, the effect is accentuated for smaller volumes. Additionally, the onset of fracture in silicon nanoparticles is bracketed by repeat loading and imaging of nanospheres with scanning probe microscopy. Based on critically sized defects in the oxide film that passivates the silicon nanoparticles, fracture toughness for a 20-nm-radius particle is found to increase by a factor of 4 when compared to bulk silicon. Corresponding strain energy release rates increase by more than an order of magnitude and compare to first order with estimates from shielding dislocations produced during the prior loading history.

ACKNOWLEDGMENTS

This work was supported by the National Science Foundation under Grants Nos. DMI 0103169 and CMS-0322436 an NSF-IGERT program through Grant No. DGE-0114372.

[1] W. W. Gerberich, W. M. Mook, C. R. Perrey, C. B. Carter, M. I. Baskes, R. Mukherjee, A. Gidwani, J. Heberlein, P. H. McMurry, and S. L. Girshick, J. Mech. Phys. Solids **51**, 979 (2003).
[2] W. M. Mook, J. M. Jungk, M. J. Cordill, N. R. Moody, Y. Sun, Y. Xia, and W. W. Gerberich, Z. Metallkd. **95**, 6416 (2004).
[3] J. D. Nowak, W. M. Mook, A. M. Minor, W. W. Gerberich, and C. B. Carter, Philos. Mag. **87**, 29 (2007).
[4] S. X. Mao, M. Zhao, and Z. L. Wang, Appl. Phys. Lett. **83**, 993 (2003).
[5] X. Li, H. Gao, C. J. Murphy, and K. K. Caswell, Nano Lett. **3**, 11 1495 (2003).
[6] K. J. Van Vliet, J. Li, T. Zhu, S. Yip, and S. Suresh, Phys. Rev. B **67**, 104105 (2003).
[7] J. A. Moriarty, J. F. Belak, R. E. Rudd, P. Soderlind, F. H. Streitz, and L. H. Yang, J. Phys.: Condens. Matter **14**, 2825 (2002).
[8] S. Veprek and A. S. Argon, J. Vac. Sci. Technol. B **20**, 650 (2002).
[9] K. F. Jarausch, J. D. Kiely, J. E. Houston, and P. E. Russell, J. Mater. Res. **15**, 81693 (2000).
[10] R. Astala, M. Kaukonen, R. M. Nieminen, and T. Heine, Phys. Rev. B **61**, 2973 (2000).
[11] W. Wang, Mater. Trans., JIM **42**, 4 606 (2001).
[12] W. C. Oliver and G. M. Pharr, J. Mater. Res. **7**, 1564 (1992).
[13] F. Murnaghan, *Finite Deformation in an Elastic Solid* (Dover, New York, 1967); Murnaghan's integrated linear equation of state, in J.-P. Poirier, *Introduction to the Physics of the Earth's Interior*, 2nd ed. (Cambridge University Press, Cambridge, England, 2000), pp. 65, 77.
[14] F. D. Stacey and P. M. Davis, Phys. Earth Planet. Inter. **142**, 137 (2004).
[15] S. Speziale, C.-S. Zha, and T. S. Duffy, J. Geophys. Res., [Solid Earth] **106**, 515 (2001).
[16] N. E. Christensen, A. L. Ruoff, and C. O. Rodriguez, Phys. Rev. B **52**, 9121 (1995).
[17] R. Pandey, M. Causa, N. M. Harrison, and M. Seel, J. Phys.: Condens. Matter **8**, 3993 (1996).
[18] A. M. Minor, E. T. Lilleodden, M. Jin, E. A. Stach, D. C. Chrzan, and J. W. Morris, Jr., Philos. Mag. **85**, 323 (2005).
[19] H. Hertz, J. Reine Angew. Math. **92**, 156 (1881).
[20] K. Johnson, *Contact Mechanics* (Cambridge University Press, Cambridge, England, 1985), p. 57.
[21] Daniel Errandonea, Y. Meng, M. Somayazulu, and D. Hausermann, Physica B **355**, 116 (2005).
[22] W. W. Gerberich, M. J. Cordill, W. M. Mook, N. R. Moody, C. R. Perrey, C. B. Carter, R. Mukherjee, and S. L. Girschick, Acta Mater. **53**, 2215 (2005).
[23] J. -S. Wang and Z. Suo, Acta Metall. Mater. **38**, 7 1279 (1990).
[24] P. H. Shipway and I. M. Hutchings, Philos. Mag. A **67**, 6 1389 (1993).
[25] R. Majzoub and M. Munawar Chaudhri, Philos. Mag. Lett. **80**, 6 (2000); **80**, 387 (2000).
[26] O. L. Warren, S. A. Downs, and T. J. Wyrobek, Z. Metallkd. **95**, 5 287 (2004).
[27] C.-F. Qian and J. C. M. Li, Mech. Mater. **24**, 1 1 (1996).